Rearranging Fluorescence-Magneto Spatiality for "Win-Win" Dual Functions to Enhance Point-of-Care Diagnosis

Yu Su[1], Xirui Chen[1], Huan Huang[2], Yuhao Wu[1], Xuan-ang Shen[1], Xiangkai Lin[1], Kun Sun[1], Xiao-Yong Fan[2], Xiaolin Huang[1], and Yonghua Xiong[1]

[1]Nanchang University
[2]Fudan University

September 25, 2023

Abstract

Fluorescent-magneto nanoemitters have gained considerable attention for their applications in mechanical controlling-assisted optical signaling. However, the incompatibility between magnetic and fluorescent components often leads to functional limitations in traditional magneto@fluorescence nanostructure. Herein, we introduce a new compact-discrete spatial arrangement on a "fluorescence@magneto" core–shell nanostructure consisting of a close-packed aggregation-induced emission luminogen (AIEgen) core and a discrete magnetic shell. This structural design effectively eliminates the optical and magnetic interferences between the dual components by facilitating AIEgens loading in core region and reducing the magnetic feeding amount through effective exposure of the magnetic units. Thereby, the resulting magneto-AIEgen nanoparticle (MANP) demonstrates "win-win" performances: (i) high fluorescent intensity contributed by AIEgens stacking-enhanced photoluminescence and reduced photons loss from the meager magnetic shell; (ii) marked magnetic activity due to magneto extraposition-minimized magnetic shielding. Accordingly, the dual functions-retained MANP provides a proof of concept for construction of an immunochromatographic sensing platform, where it enables bright fluorescent labeling after magnetically enriching and separating procalcitonin and lipoarabinomannan in clinical human serum and urine, respectively, for the clinical diagnosis of bacterial infections-caused inflammation and tuberculosis. This study not only inspires the rational design of magnetic-fluorescent nanoemitter, but also highlights promising potential in magneto-assisted point-of-care test and biomedicine applications.

Yu Su[1, 2], Xirui Chen[1, 2], Huan Huang[4, 5], Yuhao Wu[1, 2], Xuan-ang Shen[1, 2], Xiangkai Lin[1, 2], Kun Sun[1, 2], Xiao-Yong Fan[4, *], Xiaolin Huang[1, 2, *] and Yonghua Xiong[1, 2, 3, *]

[1] Dr. Y. Su, Dr. X. Chen, Y. Wu, X. Shen, X. Lin, K. Sun, Prof. X. Huang, Prof. Y. Xiong

State Key Laboratory of Food Science and Resources, Nanchang University, Nanchang 330047, P. R. China

E-mail: xiaolin.huang@ncu.edu.cn; xiongyonghua@ncu.edu.cn

[2] Dr. Y. Su, Dr. X. Chen, Y. Wu, X. Shen, X. Lin, K. Sun, Prof. X. Huang, Prof. Y. Xiong

School of Food Science and Technology, Nanchang University, Nanchang 330047, P. R. China

[3] Prof. Y. Xiong

Jiangxi-OAI Joint Research Institute, Nanchang University, Nanchang 330047, P. R. China

H. Huang, Prof. X.-Y. Fan

1

Shanghai Institute of Infectious Disease and Biosecurity, Shanghai Public Health Clinical Center, Fudan University, Shanghai 200032, China

E-mail: xyfan008@fudan.edu.cn

H. Huang

Shanghai Key Laboratory of Atmospheric Particle Pollution Prevention, Department of Environmental Science & Engineering, Fudan University, Shanghai 200438, China

Abstract: Fluorescent-magneto nanoemitters have gained considerable attention for their applications in mechanical controlling-assisted optical signaling. However, the incompatibility between magnetic and fluorescent components often leads to functional limitations in traditional magneto@fluorescence nanostructure. Herein, we introduce a new compact-discrete spatial arrangement on a "fluorescence@magneto" core–shell nanostructure consisting of a close-packed aggregation-induced emission luminogen (AIEgen) core and a discrete magnetic shell. This structural design effectively eliminates the optical and magnetic interferences between the dual components by facilitating AIEgens loading in core region and reducing the magnetic feeding amount through effective exposure of the magnetic units. Thereby, the resulting magneto-AIEgen nanoparticle (MANP) demonstrates "win-win" performances: (i) high fluorescent intensity contributed by AIEgens stacking-enhanced photoluminescence and reduced photons loss from the meager magnetic shell; (ii) marked magnetic activity due to magneto extraposition-minimized magnetic shielding. Accordingly, the dual functions-retained MANP provides a proof of concept for construction of an immunochromatographic sensing platform, where it enables bright fluorescent labeling after magnetically enriching and separating procalcitonin and lipoarabinomannan in clinical human serum and urine, respectively, for the clinical diagnosis of bacterial infections-caused inflammation and tuberculosis. This study not only inspires the rational design of magnetic-fluorescent nanoemitter, but also highlights promising potential in magneto-assisted point-of-care test and biomedicine applications.

1. Introduction

The emergence of multifunctional materials (MFMs) that integrate multiple functions into a single hybrid has revolutionized nano-operation and expanded the range of applications.[1-4] Ideal MFMs should meet two main criteria: (i) maximize synthesis efficiency and minimize inactive components by adhering to the principle of "atom economy", and (ii) achieve maximal integrated functionalities, known as "multifunctional efficiency".[5,6] However, achieving excellent multiperformance in a single composite remains challenging due to the mismatch of physicochemical properties and mutual interferences among functional building blocks.[7,8]

Fluorescent-magneto nanoemitters (FMNs), as a typical type of MFM, combine luminous and magnetic properties, enabling brilliant optical signaling and mechanical magnetic manipulation. FMNs find widespread applications in sensing,[9-11] imaging,[12,13] biomedicine,[14,15] information decoding,[16] environmental treatment,[17,18] nanorobot operation[19,20] and catalysis.[21] Over the past decades, various synthesis strategies have been proposed for FMNs.[22-25] For example, a layer-by-layer assembly approach has been applied to synthesize FMNs by electrostatically attracting oppositely charged polyelectrolytes and CdTe quantum dots (QDs) on the surface of Fe_3O_4 nanoparticles.[26] However, the weak binding affinity resulting from electrostatic interactions often leads to detachment of the exterior fluorescent particles from the FMNs. Another approach, introduced by Huang *et al.*, involves the chemical coupling of Fe_3O_4 core@silica shell@QDs satellites,[27] which improves colloid stability but compromises the loading capacity of fluorescent materials. In a remarkable advancement, Hu's lab reported an affinity-driven assembly of Fe_3O_4 nanoparticles and QDs in radial dendritic silica colloids, achieving high packing density.[28] These developed MFMs exhibit a typical "magneto@fluorescence" core–shell structure, where the exterior QD layer causes severe magnetic shielding effects on the interior magnetic core.[29,30] Therefore, increasing the loading of magnetic units becomes necessary to maintain magnetic manipulation capability. However, excessive magnetic

material loading can lead to fluorescent quenching due to the inner-filter effect (IFE) because the broad absorption of the magnetic component in the ultraviolet–visible (UV–vis) light region overlaps with the excitation and emission spectra of the existing fluorescent emitter.[31] In applications, such as lateral flow immunoassay (LFIA) detection, the mutual interference within FMNs poses a longstanding challenge. When a large amount of magnetic components stacks on a nitrocellulose (NC) membrane in the strip, it can cause nonlinear increments between the fluorescence signal and FMN content on the test and control line zones, thereby reducing the accuracy of the strip and potentially resulting in false negative results.

In theory, the rational spatial arrangement of FMNs with a novel "fluorescence@magneto" core–shell structure can effectively expose the magnetic units and reduce magnetic shielding, thereby decreasing the demand for magnetic loading and alleviating fluorescent IFE. Consequently, a worthy attempt is to decrease the exterior magneto loading while increasing the interior fluorophore content to achieve dual-retained activities. Moreover, ensuring a discrete spatial distribution of the magnetic layer is crucial to provide sufficient space for efficient photoluminescence process. Therefore, controlled phase separation in the nanometer regime through co-assembly becomes highly desirable.[32,33] For instance, in our previous work,[34] oleic acid-modified CdSe/ZnS QDs and Fe_3O_4 nanoparticles were successfully encapsulated into two polymer matrixes with different hydrophobic properties using a simple phase separation assembly. In this case, the magnetic and fluorescent components were mainly distributed in the outer layer, achieving a discrete co-display distribution that maintained high saturation magnetization due to the outward location of magnetic subunits. However, this approach sacrificed the large packing space inside the particle for fluorescent material because the maximized fluorophore coverage on the exterior interface was still not abundant enough to achieve a more enhanced fluorescent signal. Moreover, spatial separation of the two components is advantageous in minimizing multicomponent interference.[35] In addition, organic fluorescent emitters or inorganic fluorescent materials often suffer from the aggregation-caused quenching effect at high fluorophore concentrations or in the solid state, which hinders the enhancement of fluorescent brightness in compactly packed FMN hybrids.[36-38] By contrast, luminogens with aggregation-induced emission (AIEgens),[39,40]characterized by propeller-shaped structures, provide an excellent choice for remarkably increasing molecule loading and enhancing fluorescent intensity.

In this study, we present a novel compact-discrete "fluorescence@magneto" spatial arrangement by incorporating AIEgens into the core and hydrophobic Fe_3O_4 nanoparticles into the polymer shell (**Scheme 1**). This rational spatial design of the magneto-AIE nanoparticle (MANP) largely reduces magnetic shielding on the exterior magnetic shell, enabling a lower magnetic feeding amount. Consequently, the fluorescent performance is effectively maintained because of AIE-enhanced photoluminescence, a large AIEgen loading capacity, and reduced IFE by the meager magnetic shell. Capitalizing on the dual-retained magnetic and fluorescent properties, the MANP was employed as a bifunctional LFIA nanoprobe (MANP-LFIA) to magnetically enrich, separate, and fluorescently label procalcitonin (PCT) in serum samples and lipoarabinomannan (LAM) in urine samples of tuberculosis (TB) patients with remarkably enhanced sensitivity. We believe that the proposed MANP offers a new approach for the design of highly performing FMNs and holds great potential for applications in point-of-care test (POCT), fluorescent-magnetic resonance dual-mode imaging, and magnetically manipulated biomedicine.

Results and Discussion

2.1. Synthesis and Characterization of the Compact-Discrete MANP.

The fabrication of MANP involved a one-pot emulsification and evaporation method, where superparamagnetic Fe_3O_4 NPs@OA (**Figure S1**) and red-emitting AIEgens (**Figure S2**) were co-assembled as functional units, along with poly(maleicanhydride-alt-1-octadecene) (PMAO) polymer as the supporting skeleton. In this process, 6 mg of hydrophobic Fe_3O_4 NPs@OA, 6 mg of AIEgens, and 5 mg of PMAO were dissolved in chloroform and underwent micellar encapsulation in an aqueous phase using sodium dodecyl sulfate (SDS) as a surfactant. During the evaporation of chloroform, the components (Fe_3O_4 NPs@OA, AIEgens, and PMAO) self-assembled and co-constructed a spherical nanocomposite called $MANP_{6:6}$. Scanning electron microscopy (SEM) image (**Figure 1** a) and transmission electron microscopy (TEM) image (**Figure 1** b)

demonstrate the homogeneous spherical morphology of MANP$_{6:6}$. The magnified TEM image (**Figure1** c) clearly shows a core–shell nanostructure with a compact AIE core and a discretely packed Fe$_3$O$_4$NPs@OA shell, indicating a phase separation process within MANP$_{6:6}$ due to the different polarities of the building blocks. By contrast, PMAO polymer nanoparticles (PNP), AIE nanoparticles (ANP$_6$), and magnetic nanoparticles (MNP$_6$) were synthesized as single functional component analogs. TEM image in**Figure 1** d reveals the solid spherical structure of PNP. However, ANP$_6$ displays a distinct AIE core-PMAO shell structure due to the polarity difference between AIEgens and the polymer (**Figure 1** e). **Figure 1** f shows that MNP$_6$ exhibits a spherical geometry with Fe$_3$O$_4$ NPs@OA homogeneously distributed throughout the nanoparticle, owing to the high compatibility between OA and PMAO. These results support the reasonable formation mechanism of MANP: (i) the high mutual affinity between OA, PMAO, and SDS leads to the uniform assembly of Fe$_3$O$_4$ NPs@OA on the exterior PMAO shell, close to the SDS aqueous phase, with a discrete distribution; (ii) the aromatic AIEgens tend to migrate to the particle center and aggregate together due to their incompatible molecular affinity with the shell components.

Furthermore, **Figure 1** g shows that MANP$_{6:6}$ exhibits the characteristic UV–vis spectrum of ANP$_6$ and demonstrates an absorption lift in the 200–600 nm range due to the incorporation of the magnetic component. By contrast, PNP exhibits negligible light absorption, indicating that the polymer matrix does not contribute to optical interference in MANP$_{6:6}$. The energy dispersive X-ray (EDX) elemental mapping images display the distribution of C, Fe, O, and S in MANP$_{6:6}$. **Figure 1** h shows that the C elements are primarily concentrated in the core position, Fe and O elements are located on the exterior shell, and S elements are uniformly distributed throughout MANP$_{6:6}$. Further EDX line scan (**Figure 1** i) across the center of MANP$_{6:6}$ confirms the presence of a nuclear C core and an out-layer Fe, verifying the distinct assembling spatiality of Fe$_3$O$_4$ NPs@OA and AIEgens in the core–shell magnetic-fluorescent MANP$_{6:6}$. X-ray photoelectron spectroscopy (XPS) analysis (**Figures 1** j, k,**Figure S3**) implies the co-existence of C, O, and Fe in MANP$_{6:6}$. In addition, the powder X-ray diffraction (XRD) analysis (**Figure 1** l) reveals characteristic diffraction peaks corresponding to the (220), (311), (400), (511), and (440) planes of superparamagnetic Fe$_3$O$_4$crystal, suggesting the successful loading of Fe$_3$O$_4$ NPs@OA in MANP$_{6:6}$. Dynamic light scattering measurements show that MANP$_{6:6}$is well-monodispersed with a uniform hydrodynamic size of ~320 nm (**Figure 1** m). Moreover, the surface of MANP$_{6:6}$ becomes predominantly negatively charged after the carboxylation process, which is beneficial for subsequent biomodification (**Figure 1** n). The fluorescent spectra demonstrate that MANP$_{6:6}$ exhibits maximum excitation wavelengths at 365 and 465 nm, with a maximum emission peak at 600 nm (**Figure S4**). This red-light emitter property enables MANP$_{6:6}$ to effectively resist biological interference. Collectively, these results provide strong evidence for the successful construction of MANP.

2.2. "Win-Win" Magneto-Fluorescent Performances of MANP.

The magneto-fluorescent performance of MANP is influenced by its well-defined spatial structure, including the compact AIE core, discrete magneto shell, and the composition ratio of its functional components. Therefore, a rational regulation of the optical and magnetic integration in MANP was conducted to achieve dual-retained performances. SEM and TEM images shown in **Figures 2** a–c and **Figure S5**demonstrate that by increasing the feeding amount of Fe$_3$O$_4$ NPs@OA from 2 mg to 16 mg while keeping the AIEgens mass at 6 mg, the MANP$_{2:6}$, MANP$_{4:6}$, MANP$_{6:6}$, MANP$_{8:6}$, and MANP$_{16:6}$ maintain the core–shell nanostructure. However, an increase in Fe$_3$O$_4$ NPs@OA content results in gradual surface roughness and denser magnetic inlay. The increased magnetic feeding also leads to higher UV–vis absorbance of the synthesized MANP due to the intrinsic optical absorption of Fe$_3$O$_4$ NPs@OA (**FigureS6**). Fluorescent lifetime measurements show negligible lifetime decay when incorporating 6 mg or 16 mg Fe$_3$O$_4$ NPs@OA into MANP in comparison to ANP$_6$ (**Figure 2** d). These results imply the occurrence of a fluorescent IFE in MANP, which inevitably quenches the final fluorescent emission. As validated in **Figure2** e, a higher proportion of magnetic component corresponds to a gradually decreased fluorescent signal. Additionally, **Figures 2** f and **S7** show that the magnetic recovery of MANP under an external magnetic field increases with the amount of Fe$_3$O$_4$ NPs@OA and reaches a plateau at a Fe$_3$O$_4$ NPs@OA content of 6 mg. On the basis of these observations, the fluorescent intensity of MANP$_{6:6}$ exhibits a much higher retention rate of 82%, which is

much higher than the traditionally reported "magneto@fluorescence" core-shell nanostructure possessing a fluorescent retention rate below 50%.[41] This can be attributed to the outstanding luminescence property of AIEgens in an aggregated state and the discrete distribution of Fe_3O_4 NPs@OA that enables effective passage of photons through the polymer shell layer. Therefore, simultaneous high magneto-fluorescent activities can be achieved by constructing $MANP_{6:6}$ with magnetic and fluorescent of 6 mg each.

The magnetic performance of the well-emitted $MANP_{6:6}$ was evaluated. As shown in **Figure 3** a, MNP_6 and ANP_6 exhibit either magnetic or fluorescent responsiveness, respectively, due to their single functional component. By contrast, $MANP_{6:6}$ can be readily collected and exhibits bright fluorescence under an external magnetic field and UV light source. The magnetization curves in **Figure 3** b quantify that $MANP_{6:6}$ exhibits superparamagnetism with a saturation magnetization of 24.8 emu g^{-1}, which is remarkably higher than that of MNP_6 (20.9 emu g^{-1}). This indicates that the solid structure of MNP_6, with Fe_3O_4 NPs@OA filling the interior of the nanoparticle, can suffer from a magnetic shielding effect caused by the nonmagnetic dielectric polymer matrix.[42] In the contrastive case of $MANP_{6:6}$, the well-defined core–shell nanostructure allows the magnetic constituent to spread over the exterior shell while the AIEgens occupy the inner core space. This leads to a highly retained saturation magnetization. In other words, the rational spatial distribution of Fe_3O_4 NPs@OA on the exterior shell layer effectively guarantees the magnetic performance of $MANP_{6:6}$, curtails magnetic constituent to suppress fluorescent quenching, and improves optical sensitivity. Thus, the constructed $MANP_{6:6}$ possesses excellent dual functionality with simultaneous high magnetic manipulation and optical output activity.

To further evaluate the fluorescent feasibility of the nanoparticles on paper test strips, we also investigated the IFE of $MANP_{6:6}$ on the strip by spraying a series of particle concentration of $MANP_{6:6}$ on the NC membrane as the T line. As presented in **Figures 3** c, d, the fluorescent brightness of $MANP_{6:6}$ shows a synchronized tendency with that of ANP_6, with a limit of detection (LOD) of 42 ng mL^{-1} particle concentration. Moreover, negligible fluorescent decay of $MANP_{6:6}$ and ANP_6 occurs at a high particle concentration of 2.8 mg mL^{-1} (~0.8 μg/strip). This indicates that the particle stacking process on the NC membrane does not generate an obvious fluorescent IFE owing to the reduced magnetic loading amount in $MANP_{6:6}$. The effective avoidance of IFE is thus crucial in LFIA detection (~0.6 μg/strip in further POCT sensors). Furthermore, the versatility of the synthesis strategy was confirmed by individually incorporating green or yellow AIEgens (**Figures S8** a, b) into the nanoparticles. As shown in**Figures S8** c–f, the obtained green, yellow, and red $MANP_{6:6}$ emit characteristic fluorescence signals at 500, 545, and 600 nm. Confocal laser scanning microscope imaging results (**Figure S8** g) demonstrate that multicolor spheres with single-particle brightness can be visualized simultaneously under a single excitation. This indicates that the proposed MANP holds great potential for multicolor fluorescent imaging and high-throughput multiplex detection.

Given the excellent combination of magnetic and fluorescent performance, $MANP_{6:6}$ shows promise as a dual-functional nanoprobe for bioanalytical applications. The following investigations were conducted to ensure its stability in further bioapplications. As shown in**Figure 3** e, $MANP_{6:6}$ exhibits slight fluorescent decrease and hydrodynamic size increase in acidic or basic conditions, with negligible change in magnetic recovery across pH values ranging from 2 to 11. These results indicate that $MANP_{6:6}$ maintains good optical, magnetic, and colloid stability over a wide pH range, making it suitable for various biochemical applications. Furthermore, the thermal stability of $MANP_{6:6}$ was evaluated by storing the particles at 60 °C for one week. As depicted in **Figure 3** f, $MANP_{6:6}$ demonstrates excellent optical, magnetic, and colloid stability under elevated temperatures, indicating superior long-term stability. In addition, the stability of $MANP_{6:6}$ in biological matrices was examined by incubating the particles in PB, human serum, and human urine for 7 days. As shown in **Figures 3** g–i, $MANP_{6:6}$ exhibits stable fluorescent signals, consistent magnetic recoveries, and high colloid stability in PB, serum, and urine media over the course of 7 days. Taken altogether, these results demonstrate the excellent colloid, optical, magnetic, and thermal stability of $MANP_{6:6}$, which is vital for its multifunctional bioanalytical application, enabling simultaneous magnetic separation, enrichment, and fluorescent signal output.

2.3. POCT Applications of MANP in Ultrasensitive Immunochromatographic Detection.

The remarkable magneto-fluorescence retention and prominent stability of MANP$_{6:6}$ make it practical for biomedical applications. In this study, we further investigated the feasibility of MANP$_{6:6}$ as a dual-functional magnetic separation and fluorescent nanoprobe in the field of POCT, specifically using LFIA as the detection platform. **Scheme 1** depicts the construction principle of the MANP-FLIA platform for ultrasensitive detection of targets in human serum/urine. The assay is based on a double-antibody sandwich immunoassay format. When the targets are present in serum or urine, the antigens are initially bound to monoclonal antibodies modified MANP$_{6:6}$ (MANP$_{6:6}$@mAbs), forming a MANP$_{6:6}$@mAbs immunocomplex. The immunocomplex is then collected by an external magnetic field and resuspended in buffer solution. The complex solution was then applied to the LFIA test strip, which has antibodies immobilized on the NC membrane. This results in the formation of a nanoprobe/antigen/antibody sandwich architecture on the T line with high fluorescent signals (FI$_T$). Additionally, excess MANP$_{6:6}$@mAbs are captured by the goat anti-mouse IgG on the C line, producing a corresponding fluorescent signal (FI$_C$). In the absence of the targets, the MANP$_{6:6}$@mAbs run to the C line and react with the IgG. The presence or absence of fluorescent lines provide a direct visual diagnosis result: one line (C) indicates a negative result for the targets, whereas two lines (T + C) indicate a positive result. In addition, the ratio of FI$_T$/FI$_C$ is used to accurately quantify the target concentration, which effectively circumvents the intensity fluctuations by employing a ratiometric strategy.

2.3.1. PCT Detection in Human Serum Samples.

PCT was selected as the serum target, which is a biomarker of sepsis and pyemia caused by bacterial infection. Accurate monitoring of PCT at low concentration ranges is of great importance for indicating the degree of inflammation and guiding antibiotic therapy.[43,44] To begin with, the coupling conditions of the MANP$_{6:6}$@PCT-mAbs were adjusted to optimize the final performance. This optimization included adjusting the coupling pH of PCT-mAbs, the amount of EDC used, and the saturated labeling amount of anti-PCT mAbs on MANP$_{6:6}$ (**Figures S** 9a–c). As shown in **Figure S9** d, the as-obtained MANP$_{6:6}$@PCT-mAbs nanoprobes exhibited good monodispersity with a slight size increase of 20 nm compared with that of MANP$_{6:6}$. Additionally, the zeta potential of MANP$_{6:6}$@PCT-mAbs was decreased by 23.7 mV, due to the presence of the PCT-mAbs with negative charge (**FigureS9** e). These observations demonstrate the successful modification of antibodies on the MANP$_{6:6}$. Moreover, the as-fabricated MANP$_{6:6}$@PCT-mAbs probes maintained the fluorescent profile and brightness (**Figure S9** f), which remarkably ensured the detection sensitivity of the LFIA strip. Besides, maximum responses were further obtained by optimizing the strip and running parameters, such as the sprayed concentration of PCT-mAbs on the T line, the added amount of MANP$_{6:6}$@PCT-mAbs probes for each strip, the immunoreaction time, and the magnetic separation volume (**Figures S10** a–d). Furthermore, the serum dilution volume was investigated to achieve the best immunoreaction and magnetic capture efficiency in practical samples. As revealed in **Figure S10** e, the fluorescent intensity increases with the dilution degree, and a signal plateau is reached with a twofold serum dilution, effectively eliminating serum matrix interference on the immunoreaction and LFIA fluorescent reading.

Under the developed conditions mentioned above, PCT standards in serum solutions with various concentrations were magnetically enriched and detected using MANP$_{6:6}$@PCT-mAbs probes-immunolabeled LFIA test strips. As shown in **Figure 4** a, the fluorescent signal on the T line gradually increases as the concentration of PCT increases, followed by a decrease in the fluorescent signal on the C line. The logarithm of the ratiometric FI$_T$/FI$_C$ linearly increases with the logarithm of the antigen concentration in the range from 0.0018 ng mL^{-1} to 62.5 ng mL^{-1}, as shown in**Figure** 4b. The linear regression equation for PCT in serum is$Y = 0.9992\ X^{\ 0.7798}$, where Y represents the logarithm of FI$_T$/FI$_C$, and X is the logarithm of PCT concentration, with a linear regression coefficient of 0.9977. The LOD of this method for PCT was determined to be 0.0012 ng mL^{-1} (defined as the concentration corresponding to 20 negative means plus triple standard deviation). In comparison, direct detection of PCT in serum without magnetic separation resulted in a liner responding range (0.0075–62.5 ng mL^{-1}, $R^{\ 2} = 0.9947$) with a higher LOD of 0.0068 ng mL^{-1}(**Figures 4** b, **S11**). Moreover, a traditional AuNPs-based colorimetric LFIA (AuNPs-LFIA) was constructed, which showed a much narrower liner responding range (0.06–15.6 ng mL^{-1},$R^{\ 2} = 0.9826$) and a

higher LOD of 0.06 ng mL^{-1} (**Figures 4** b, **S12**). This indicates a 5.6-fold and 50-fold higher sensitivity of the magnetic-assisted MANP-LFIA compared with MANP-LFIA without magnetic operation and AuNPs-LFIA, demonstrating the remarkable superiority of the developed sensor in detecting trace targets. Furthermore, the upper limit of PCT detection by magnetic-assisted MANP-LFIA is lifted by four times compared with that of AuNPs-LFIA, which is highly important to severe inflammation diagnosis. Such excellent analytical performance is attributable to the magnetic operation, which effectively enriches the PCT protein from a larger sample volume to obtain a higher target amount and extracts the PCT from the serum to mitigate matrix interference, and high fluorescent brightness of MANP$_{6:6}$ with weak IFE.**Figure 4** c shows the typical strip prototypes after the detection of various concentration (0–250 ng mL^{-1}) of PCT-spiked serum samples. Clearly, the brightness of the T lines remarkably increases with an increasing concentration of the target. The particle location was also confirmed by SEM. As shown in **Figure4** d, masses of MANP$_{6:6}$@PCT-mAbs are immobilized tightly on the NC fiber in the T line region in the case of a PCT concentration of 100 ng mL^{-1}, whereas negligible nonspecific adsorption is observed on the NC membrane in the PCT-negative sample, which matches well with the visual result. These results demonstrate that the proposed MANP-FLIA provided good sensitivity for POCT detection, and the paper strip platform provides visual analysis of biomarker monitoring. The detection specificity is also a key issue in immunoassays. Here, hepatitis B surface antigen (HBsAg), prostate-specific antigen (PSA), human chorionic gonadotropin (HCG), HIV p24 antigen, carcinoembryonic antigen (CEA), α-fetoprotein (AFP), N-terminal prohormone of brain natriuretic peptide (NT-ProBNP), and C-reactive protein (CRP) were selected as the interfering proteins to evaluate the selectivity of the immunoassay platform. The FI$_T$/FI$_C$ of PCT at 1 ng mL^{-1} was compared with those of interference species at the 1000 ng mL^{-1} concentration level. As shown in the spider diagram in **Figure 4** e and photograph in**Figure S13** , a negligible signal was detectable in the interference species, whereas a strong fluorescent signal was observed in the PCT sample. This result demonstrates that the proposed MANP-FLIA platform exhibits good specificity to the target protein and has the ability to differentiate it from complex samples. In addition, the accuracy and precision of the MANP-LFIA method were investigated by determining the intra- and inter-assay recoveries and percent coefficients of variation (%CVs) of seven PCT-spiked serum samples with concentrations of 0.05, 0.1, 0.5, 1, 5, 10, and 50 ng mL^{-1}. As revealed in **Table S1** , the average recoveries of the intra-assay ranged from 84.7% to 105.6% with CVs ranging from 3.49% to 9.66%, and the average recoveries of the inter-assay ranged from 85.2% to 96.3% with CVs ranging from 7.3% to 14.4%. These results indicate that the proposed MANP-LIFA is suitable for accurate PCT quantification with satisfactory precision.

Furthermore, we demonstrated the reliability and practicability of the proposed method by measuring 34 human blood plasma samples from patients. As shown in **Figure 4** f and **Table S2** , the detection results showed a high level of agreement compared with those measured by commercial chemiluminescence immunoassay (CLIA) kits, without any false-positive or false-negative signals. On this basis, a regression analysis was conducted between the proposed method and the standard CLIA by the hospital. **Figure 4** g demonstrates a strong positive correlation between the MANP-FLIA method and the standard CLIA, with correlation coefficients of 0.966. These results confirm that the proposed method is accurate and valid for clinical diagnosis.

2.3.2. *LAM Detection in Human Urine Samples.*

Encouraged by the excellent analytical performance of MANP-LFIA in serum matrix, we further evaluated its universality in another noninvasive body fluid, urine samples. Lipoarabinomannan (LAM), a mycobacterial-specific glycolipid shed into urine during active tuberculosis (TB), has been confirmed as a promising TB biomarker that can facilitate TB diagnosis and guide TB treatment.[45-47] We selected LAM as the target for the urinary diagnosis of TB to demonstrate the superiority of our developed MANP-LFIA. The non-sputum POCT method was based on the specific recognition of LAM in urine using a pair of monoclonal antibodies (A12 and A1) on the sensing strip. To optimize the magnetic separation-assisted MANP-LFIA for achieving the best sensitivity for LAM detection on the strip nanobiosensor, we systematically investigated and optimized the probe fabrication parameters, including the coupling pH of A1 mAbs, EDC amount, saturated labeling amount of A1 mAbs on MANP$_{6:6}$, and the immunoreaction conditions, such as sprayed

concentration of A12 mAbs on the T line, added amount of $MANP_{6:6}$@A1 mAbs probes for each strip, immunoreaction time, running buffer, magnetic separation volume, and urine dilution volume (**Figure S14**).

On the basis of these optimal conditions, a series of urine solutions spiked with LAM in the concentration range of 0 ng mL^{-1} to 20 ng mL^{-1} were determined using our developed MANP-LFIA platform. As displayed in typical strip prototypes in **Figure 5** a, the fluorescent brightness of the T lines gradually increased as the concentrations of the target LAM increased, showing target concentration-dependent fluorescent signal changes. The MANP-LFIA with magnetic operation presented a more readily visual signal on the T line at low target concentration level compared with that without magnetic assistance. Higher ratiometric FI_T/FI_C signals were observed in MANP-LFIA with magnetic operation (**Figure 5** b), indicating the unique superiority of the dual-functional MANP in enriching LAM and avoiding urine interference. Our magnetic operation-assisted strip nanobiosensor exhibited a broad linear detection range for LAM from 0.01 ng mL^{-1} to 20 ng mL^{-1} with a correlation coefficient of 0.997. The linear regression equation for LAM in urine is $Y = - 0.30791 + 0.68521\ X$, where Y represents the logarithm of FI_T/FI_C, and X is the logarithm of LAM concentration, with an LOD of 0.016 ng mL^{-1}(defined as the concentration corresponding to 20 negative means plus triple standard deviation). By contrast, the direct running of spiked urine without magnetic operation resulted in lower sensitivity with a higher LOD of 0.088 ng mL^{-1} (**Figure5** c). In addition, we constructed a traditional AuNPs-LFIA and only obtained a LOD of 0.7 ng mL^{-1} (**FigureS15**). This indicates a 5.5-fold and 44-fold higher sensitivity of the magnetic-assisted MANP-LFIA compared with MANP-LFIA without magnetic operation and AuNPs-LFIA, revealing the remarkable advantage of the developed MANP-LFIA in LAM determination.

The specificity of our developed strip biosensor toward LAM was studied by recording the responses against several common mycobacterial strains, including the target *Mycobacterium tuberculosis* H37Rv and other non-tuberculosis mycobacterial strains (*M. simiae* , *M. scrofulaceum* , *M. parascrofulaceum* , *M. moelleri* , *M. intracellulare* , *M. paraJortuitum* , *M. triviale* , *M. peregrinum* , *M. abscessus* , *M. septium* , *M. mucogenicum* , *M. avium* , *M. gilvum* , *M. chelonei* , and*M. smegmatis*) with a bacterial concentration of 2.5×10^4 CFU mL^{-1}. As shown in**Figure 5** d, all rapid-growing-mycobacteria (RGM) and the majority of slow-growing-mycobacteria (SGM) species showed negligible signal, whereas a few SGM include *M. simiae* , *M. scrofulaceum* , *M. parascrofulaceum* , *M. moelleri* , and*M. intracellulare* exhibited varying degrees of cross-reactivity with *M. tuberculosis* H37Rv. Furthermore, a series of urine sample solutions collected from 10 individual healthy individuals with LAM spiking concentrations of 0, 100, 500, and 1000 pg mL^{-1} were analyzed to explore the feasibility of our fabricated analytical platform for determining the presence of targets at different concentration levels. As presented in **Figure5** e, the batches of ratiometric signals corresponding to 100, 500, and 1000 pg mL^{-1} LAM concentrations showed significant statistical differences compared with the blank group, indicating the application potential of the developed MANP-LFIA for clinical TB diagnosis. This objective was straightforwardly achieved by analyzing clinical urine samples from TB patients who have been diagnosed positive through the standard sputum test. The MANP-LFIA diagnosis results in **Figure 5** f indicate that our method possesses the ability to differentiate cohorts of TB-positive patients and healthy individuals. These findings demonstrate a highly sensitive response of our dual functional MANP-FLIA test strip to LAM in urine, providing promising potential for the early diagnosis of TB in resource-limited settings.

3. Conclusion

In this study, we successfully addressed the challenge of performance retention in FMN by introducing a novel compact-discrete "fluorescence@magneto" spatial arrangement on the MANP. The extraposition of a magnetic shell effectively circumvents magnetic shielding, allowing for a reduced requirement of Fe_3O_4@OA amount and consequently decreasing the fluorescent IFE. Additionally, the bright fluorescence can be attributed to the high loading content of AIEgens in the core and the AIE-enhanced photoluminescence. This rational spatial arrangement enables efficient mechanical control-assisted optical signaling in a LIFA platform for PCT and LAM detection, achieving a "win-win" situation where both magnetic and fluorescent

activities are performed and validated. The analytical results demonstrate that the MANP probe minimizes interference from human serum and urine matrix while enriching the targets, resulting in remarkably increased sensitivity for the diagnosis of bacterial infection diseases, such as inflammation and TB. We suggest that the as-proposed MANP provides an alternative strategy to guide the design of FMN and holds great promise for multifunctional utilization in areas, such as POCT, fluorescence-magnetic resonance dual-mode bioimaging, and magnetically manipulated biomedicine.

4. Experimental Section

Materials : The red, green, and yellow AIEgens were generously provided by Jiangxi Weibang Biotechnology Co., Ltd. Ferric chloride ($FeCl_3*6H_2O$), ferrous chloride ($FeCl_2*4H_2O$), oleic acid (OA), SDS, 1-ethyl-3-(3-dimethylaminopropyl) carbodiimide (EDC), (PMAO, MW = 30,000-50,000 Da), casein, and bovine serum albumin (BSA) were purchased from Sigma-Aldrich. The sample pad, NC membrane, and absorbent pad were obtained from Schleicher and Schuell GmbH (Dassel, Germany). Anti-PCT monoclonal antibodies (mAbs), anti-PCT polyclonal antibodies (pAbs), PCT standards, and goat anti-mouse IgG antibodies were obtained from Hua Kui Jin Pei Biotechnology Inc. (Shanghai, China). Human serum containing PCT was collected from Jiangxi Provincial People's Hospital (Nanchang, China). Anti-LAM mAbs (A12 and A1) and LAM standards were provided by the Shanghai Public Health Clinical Center (Shanghai, China). All chemicals were of analytical grade and used as received without further purification.

Apparatus and Characterizations : Transmission electron microscopy (TEM) images and energy dispersive X-ray (EDX) images were obtained using an FEI Talos F200x at an accelerating voltage of 200 kV. Scanning electron microscopy (SEM) images were acquired using a Hitachi SU8100 scanning electron microscope (Tokyo, Japan). The hydrodynamic size distributions and zeta potentials were measured using a scientific NP analyzer (Malvern Nano ZSE, London, UK). Small angle powder X-ray diffraction (XRD) measurements were conducted on a Bruker D8 ADVANCE diffractometer using CuKα radiation (λ = 0.15405 nm). X-ray photoelectron spectroscopy (XPS) analysis was conducted using an ESCALAB25OXi spectrometer (Thermo Fisher Scientific Co., USA). UV–vis spectra were recorded using a Hitachi U-3900 spectrophotometer (Tokyo, Japan). Fluorescence spectra were collected using an F-380 fluorescence spectrophotometer (Tianjin, China). The magnetic properties were characterized using a superconducting quantum interference device at 300 K. The BioDot XYZ platform, equipped with a motion controller, a BioJet Quanti3000k dispenser, and an AirJet Quanti3000k dispenser for solution dispensing, was supplied by BioDot (Irvine, CA). The portable fluorescent strip reader was obtained from Fenghang Laboratory Instrument Co. Ltd (Hangzhou, China).

Synthesis of Fe₃O₄ NPs@OA : Fe_3O_4 NPs@OA with a diameter of ~10 nm were synthesized in accordance with a previously reported method.[42] In detail, a 150 mL aqueous solution containing 1.59 g of $FeCl_2·4H_2O$ and 2.59 g of $FeCl_3·6H_2O$ was heated to 50 °C with N_2 bubbling for 15 min. Subsequently, 12.5 mL of $NH_3·H_2O$ (25% v/v) was quickly added to the mixture under vigorous stirring at 500 rpm for 30 min, resulting in a color change from yellow to black. The formed precipitate was collected under an additional magnetic field and washed with water five times to achieve a neutral pH. The precipitate was then ultrasonically dispersed in 100 mL of water. Following that, 1.2 mL of OA was added to the dark suspension, which was stirred for 3 h at 70 °C under N_2 protection. Finally, the oily Fe_3O_4 NPs@OA product was washed with ethanol and resuspended in chloroform for further use.

Synthesis of MANP₆:₆, PNP, ANP₆, and MNP₆ : MANP$_{6:6}$ was prepared by co-assembling Fe_3O_4 NPs@OA and AIEgens into a polymer matrix using our reported emulsification method with some modifications.[42] Briefly, 5 mg of PMAO, 6 mg of Fe_3O_4 NPs@OA, and 6 mg of AIEgens were completely dissolved in 150 µL of chloroform to form an oil phase. Then, 400 µL of 0.2 mg mL^{-1} SDS solution as the aqueous phase was added to the oil phase. The mixture was emulsified *via* sonicating for 5 min (9.9 s working and 5.5 s pausing) at an ultrasound power of 114 W. The resulting solution was then vortexed and evaporated for 20 min to remove the chloroform, resulting in the assembly of Fe_3O_4 NPs@OA and AIEgens into MANP$_{6:6}$. The obtained MANP$_{6:6}$ was centrifuged at 8,000 rpm for 15 min, and the pellet was resuspended in alkaline water (pH 9) overnight to hydrolyze the anhydride of PMAO and generate carboxyl groups for further antibody coupling. The carboxylated MANP$_{6:6}$ was washed three times with distilled water, adjusting the pH to neutral each

time, by centrifugation at 8,000 rpm for 15 min. The final product was dispersed in ultrapure water for further use.

The synthesis of PNP, ANP_6, and MNP_6 followed a similar procedure to that of $MANP_{6:6}$, with the only difference being the feeding groups of PMAO, PMAO and AIEgens, and PMAO and Fe_3O_4 NPs@OA as the building blocks, respectively.

Synthesis of $MANP_{6:6}$@PCT-mAbs and $MANP_{6:6}$@LAM-mAbs : The $MANP_{6:6}$@PCT-mAbs nanoprobes were synthesized using the EDC method to form an amide bond between the carboxyl group of $MANP_{6:6}$ and the amino group of anti-PCT mAbs. The same procedure was followed for the synthesis of $MANP_{6:6}$@LAM-mAbs, with A1 antibody used as the LAM detective antibody. Briefly, 6 µg of anti-PCT mAbs was added to 400 µL of 0.01 M PB solution (pH 7.4) containing 20 µg of $MANP_{6:6}$, and the mixture was incubated for 30 min. Then, 2 µg of EDC was added to the solution and stirred for 30 min at room temperature. This step was repeated for three times. Subsequently, 7 mg of casein was used to block the unbound part of $MANP_{6:6}$ for 1 h. Finally, the mixture was centrifuged at 9,000 rpm for 5 min, and the precipitates were resuspended in 100 µL of 0.01 M PB (pH 7.4) containing 25% w/v saccharose, 1% w/v BSA, and 0.1% w/v NaN_3 and stored at 4 °C for further use.

Fabrication of MANP-LFIA Strips : The $MANP_{6:6}$-LFIA strip fabrication process, including both PCT and LAM detection, is described as follows: For PCT detection, anti-PCT pAbs (2 mg mL^{-1}) and goat anti-mouse IgG (1 mg mL^{-1}) were sprayed on the NC membrane at a density of 0.74 µL cm^{-1} as the test (T) and control (C) lines, respectively, using the ZX1000 dispensing platform. The modified NC membrane was dried at 37 °C overnight. Then, the absorbent pads, treated NC membrane, and sample pads were assembled in sequence onto the PVC backing card with an overlap, ensuring secure attachment. The assembled strip was divided into pieces with a width of 3.9 mm. The as-prepared strips were packaged in a sealed bag and stored in dry and cool conditions for further use.

For LAM detection, A12 mAbs (1 mg mL^{-1}) and goat anti-mouse IgG (2 mg mL^{-1}) were sprayed on the NC membrane.

Detection of PCT in Serum and LAM in Urine Using MANP-LFIA Strip : For PCT detection, 3 µL of $MANP_{6:6}$@PCT-mAbs nanoprobe was added to 280 µL of sample solution containing 140 µL of serum sample and 140 µL of artificial serum solution. After incubation for 5 min, the formed $MANP_{6:6}$@PCT-mAbs-PCT complex was collected using an external magnetic field for 10 min and resuspended in 70 µL of artificial serum buffer solution. Subsequently, the solution was pipetted into the sample well of the strip. After running for 20 min, the strip was scanned using a commercial fluorescence strip reader, and the fluorescence intensities (FI) at the T and C lines (denoted as FI_T and FI_C) were recorded. The standard curve was generated by plotting the correlation between the FI_T/FI_C and the target concentration of PCT.

For LAM, the obtained urine samples were first heated to 100 °C for 10 min and then centrifuged at 12,000 rpm for 2 min to remove the excess non-LAM proteins. In the detection process, 3 µL of $MANP_{6:6}$@A1 nanoprobe was added to 350 µL of sample solution containing 175 µL of urine sample and 175 µL of artificial urine solution. After incubation for 5 min, the formed $MANP_{6:6}$@A1-LAM complex was collected using an external magnetic field for 10 min and resuspended in 70 µL of artificial serum buffer solution. Subsequently, the solution was pipetted into the sample well of the strip and run for 20 min for subsequent signal reading.

Statistical Analysis : Data were presented as mean ± standard deviation (SD). The statistical differences between data were evaluated using ANOVA. "*," "**," and "***" represent $p < 0.05$, $p < 0.01$, and $p < 0.001$, respectively, indicating significance or very high significance.

Conflict of Interests

The authors declare no conflict of interests.

Ethics Statement

All serum and urine samples were obtained from healthy volunteers and patients who provided written informed consent before participation. This study was approved by the Medical Ethics Committee of The First Affiliated Hospital of Nanchang University and the Ethics Committee Review Boards of Shanghai Public Health Clinical Center and Shanghai Pulmonary Hospital.

Supporting Information

Supporting Information is available from the Wiley Online Library or from the author.

Received: ((will be filled in by the editorial staff)) Revised: ((will be filled in by the editorial staff)) Published online: ((will be filled in by the editorial staff))

References

1. Y. Chen, Z. Gao, F. Zhang, Z. Wen, X. Sun, *Exploration (Beijing)* **2022,** *2* (1), 20210112.
2. J. Yang, D. Dai, X. Zhang, L. Teng, L. Ma, Y. W. Yang, *Theranostics* **2023,** *13* (1), 295-323.
3. X. Chen, L. Ding, X. Huang, Y. Xiong, *Theranostics* **2022,** *12* (2), 574-602.
4. Y. Su, B. Yuan, Y. Jiang, P. Wu, X. Huang, J. J. Zhu, L. P. Jiang, *Chem. Sci.* **2022,** *13* (22), 6573-6582.
5. R. Freund, U. Lachelt, T. Gruber, B. Ruhle, S. Wuttke, *ACS Nano* **2018,** *12* (3), 2094-2105.
6. B. M. Trost, *Science* **1991,** *254* (5037), 1471-1477.
7. X. Zhang, Z. W. Li, Y. Wu, X. Ge, L. Su, H. Feng, Z. Wu, H. Yang, J. Song, *Angew. Chem. Int. Ed.* **2021,** *60* (32), 17647-17653.
8. X. He, Z. Zhao, L. H. Xiong, P. F. Gao, C. Peng, R. S. Li, Y. Xiong, Z. Li, H. H. Sung, I. D. Williams, R. T. K. Kwok, J. W. Y. Lam, C. Z. Huang, N. Ma, B. Z. Tang, *J. Am. Chem. Soc.* **2018,** *140* (22), 6904-6911.
9. F. Salis, A. B. Descalzo, E. Benito-Pena, M. C. Moreno-Bondi, G. Orellana, *Small* **2018,** *14* (20), 1703810.
10. J. Hu, Y. Z. Jiang, M. Tang, L. L. Wu, H. Y. Xie, Z. L. Zhang, D. W. Pang, *Anal. Chem.* **2019,** *91* (1), 1178-1184.
11. Q. J. Li, Z. Y. Liao, L. Han, L. Y. Li, Y. Song, E. Q. Song, *Adv. Funct. Mater.* **2020,** *30* (49), 2004963.
12. Z. Y. Liao, L. Han, Q. J. Li, L. Y. Li, Y. Liu, Y. Song, W. H. Tan, E. R. Song, *Adv. Funct. Mater.* **2021,** *31* (18), 2009937.
13. J. H. Li, P. Santos-Otte, B. Au, J. Rentsch, S. Block, H. Ewers, *Nat. Commun.* **2020,** *11* (1), 4259.
14. M. Zhang, T. Zheng, B. L. Sheng, F. Wu, Q. C. Zhang, W. T. Wang, J. Shen, N. L. Zhou, Y. Sun, *Chem. Eng. J.* **2019,** *373* , 1054-1063.
15. Y. Yao, P. Ding, C. Yan, Y. Tao, B. Peng, W. Liu, J. Wang, M. A. Cohen Stuart, Z. Guo, *Angew. Chem. Int. Ed.* **2023,** *62* (13), e202218983.
16. B. J. Yu, S. D. Liu, W. H. Xie, P. P. Pan, P. Zhou, Y. D. Zou, Q. Yue, Y. H. Deng, *Infomat* **2022,** *4* (5), e12289.
17. Y. Song, R. Xie, M. Tian, B. Mao, F. Chai, *J. Hazard. Mater.* **2023,** *457* , 131683.
18. S. Y. Huang, S. B. Jiang, H. W. Pang, T. Wen, A. M. Asiri, K. A. Alamry, A. Alsaedi, X. K. Wang, S. H. Wang, *Chem. Eng. J.* **2019,** *368* , 941-950.
19. B. Wang, K. F. Chan, K. Yuan, Q. Wang, X. Xia, L. Yang, H. Ko, Y. J. Wang, J. J. Y. Sung, P. W. Y. Chiu, L. Zhang, *Sci. Robot.* **2021,** *6* (52), eabd2813.

20. Y. Zhang, L. Zhang, L. Yang, C. I. Vong, K. F. Chan, W. K. K. Wu, T. N. Y. Kwong, N. W. S. Lo, M. Ip, S. H. Wong, J. J. Y. Sung, P. W. Y. Chiu, L. Zhang, *Sci. Adv.* **2019,** *5* (1), eaau9650.

21. D. Rodriguez-Padron, A. D. Jodlowski, G. de Miguel, A. R. Puente-Santiago, A. M. Balu, R. Luque, *Green Chem.***2018,** *20* (1), 225-229.

22. O. Chen, L. Riedemann, F. Etoc, H. Herrmann, M. Coppey, M. Barch, C. T. Farrar, J. Zhao, O. T. Bruns, H. Wei, P. Guo, J. Cui, R. Jensen, Y. Chen, D. K. Harris, J. M. Cordero, Z. W. Wang, A. Jasanoff, D. Fukumura, R. Reimer, M. Dahan, R. K. Jain, M. G. Bawendi, *Nat. Commun.* **2014,** *5* , 5093.

23. M. Yoon, Y. Kim, J. Cho, *ACS Nano* **2011,** *5* (7), 5417-5426.

24. J. B. Lugagne, G. Brackx, E. Seyrek, S. Nowak, Y. Sivry, L. Vitorazi, J. F. Berret, P. Hersen, G. Charron, *Adv. Funct. Mater.***2017,** *27* (31), 1700362.

25. A. J. Amali, P. Saravanan, R. K. Rana, *Angew. Chem. Int. Ed.***2011,** *50* (6), 1318-1321.

26. X. Hong, J. Li, M. J. Wang, J. J. Xu, W. Guo, J. H. Li, Y. B. Bai, T. J. Li, *Chem. Mater.* **2004,** *16* (21), 4022-4027.

27. Z. Huang, Z. J. Xiong, Y. Chen, S. Hu, W. H. Lai, *J. Agr. Food. Chem.* **2019,** *67* (10), 3028-3036.

28. L. Huang, Y. Zhang, T. Liao, K. Xu, C. Jiang, D. Zhuo, Y. Wang, H. M. Wen, J. Wang, L. Ao, J. Hu, *Small* **2021,** *17*(25), e2100862.

29. R. Chen, X. R. Chen, Y. F. Zhou, T. Lin, Y. K. Leng, X. L. Huang, Y. H. Xiong, *ACS Nano* **2022,** *16* (2), 3351-3361.

30. L. Li, L. Y. Zhang, S. X. Xing, T. T. Wang, S. R. Luo, X. Q. Zhang, C. Liu, Z. M. Su, C. G. Wang, *Small* **2013,** *9* (6), 825-830.

31. E. Z. Sheng, Y. X. Lu, Y. T. Tan, Y. Xiao, Z. X. Li, Z. H. Dai,*Anal. Chem.* **2020,** *92* (6), 4364-4370.

32. D. L. Liu, R. Aleisa, Z. P. Cai, Y. Li, Y. D. Yin, *Matter***2021,** *4* (3), 927-941.

33. K. H. Ku, J. M. Shin, H. Yun, G. R. Yi, S. G. Jang, B. J. Kim,*Adv. Funct. Mater.* **2018,** *28* (42), 1802961.

34. L. Guo, Y. Shao, H. Duan, W. Ma, Y. Leng, X. Huang, Y. Xiong, Y.,*Anal. Chem.* **2019,** *91* (7), 4727-4734.

35. S. H. Hu, X. Gao, *J. Am. Chem. Soc.* **2010,** *132*(21), 7234-7237.

36. H. A. Huang, L. X. Liu, J. G. Wang, Y. Zhou, H. A. Hu, X. L. Ye, G. C. Liu, Z. X. Xu, H. Xu, W. Yang, Y. W. Wang, Y. Peng, P. H. Yang, J. Q. Sun, P. Yan, X. H. Cao, B. Z. Tang, *Chem. Sci.* **2022,***13* (11), 3129-3139.

37. H. J. He, Y. J. Cui, B. Li, B. Wang, C. H. Jin, J. C. Yu, L. J. Yao, Y. Yang, B. L. Chen, G. D. Qian, *Adv. Mater.* **2019,***31* (6), 1806897.

38. L. Wang, R. Chen, G. Han, X. Liu, T. Huang, J. Diao, Y. Sun,*Exploration (Beijing)* **2022,** *2* (3), 20210215.

39. P. W. Zhou, K. L. Han, *Aggregate* **2022,** *3* , e160.

40. X. C. Nie, W. H. Huang, D. C. Zhou, T. Wang, X. Wang, B. Chen, X. P, Zhang, G. Q. Zhang, *Aggregate* **2022,** *3* , e165.

41. Z. Huang, J. Peng, J. J. Han, G. G. Zhang, Y. J. Huan, M. L. Duan, D. F. Liu, Y. H. Xiong, S. Q. Xia, W. H. Lai, *Food Chem.***2019,** *276* , 33-341.

42. L. W. Hao, Y. K. Leng, L. F. Zeng, X. R. Chen, J. Chen, H. Duan, X. L. Huang, Y. H. Xiong, X. Y. Chen, *Adv. Sci.* **2020,***7* (2), 1902433.

43. P. Povoa, L. Coelho, F. Dal-Pizzol, R. Ferrer, A. Huttner, A. C. Morris, V. Nobre, P. Ramirez, A. Rouze, J. Salluh, M. Singer, D. A. Sweeney, A. Torres, G. Waterer, A. C. Kalil, *Intens. Care. Med.***2023,** *49* (2), 142-153.

44. K. J. Downes, J. C. Fitzgerald, S. L. Weiss, *J. Clin. Microbiol.* **2020,** *58* (7), e01851-19.

45. P. Chen, Y. Meng, T. Liu, W. Peng, Y. Gao, Y. He, R. Qu, C. Zhang, W. Hu, B. Ying, *ACS Nano* **2023,** *17* (7), 6998-7006.

46. M. Bonnet, D. Gabillard, S. Domoua, C. Muzoora, E. Messou, S. Sovannarith, D. B. Nguyen, A. Badje, S. Juchet, D. Bunnet, L. Borand, N. Natukunda, T. H. Tran, X. Anglaret, D. Laureillard, F. X. Blanc, S. A. T. Team, *Clin. Infect. Dis.* **2023,** ciad125.

47. T. Broger, L. Koeppel, H. Huerga, P. Miller, A. Gupta-Wright, F. X. Blanc, A. Esmail, B. W. P. Reeve, M. Floridia, A. D. Kerkhoff, F. Ciccacci, M. P. Kasaro, S. S. Thit, M. Bastard, G. Ferlazzo, C. Yoon, D. J. Van Hoving, B. Sossen, J. I. Garcia, M. J. Cummings, R. M. Wake, J. Hanson, A. Cattamanchi, G. Meintjes, G. Maartens, R. Wood, G. Theron, K. Dheda, I. D. Olaru, C. M. Denkinger, T. B. S. Consortium,*Lancet Glob. Health* **2023,** *11* (6), e903-e916.
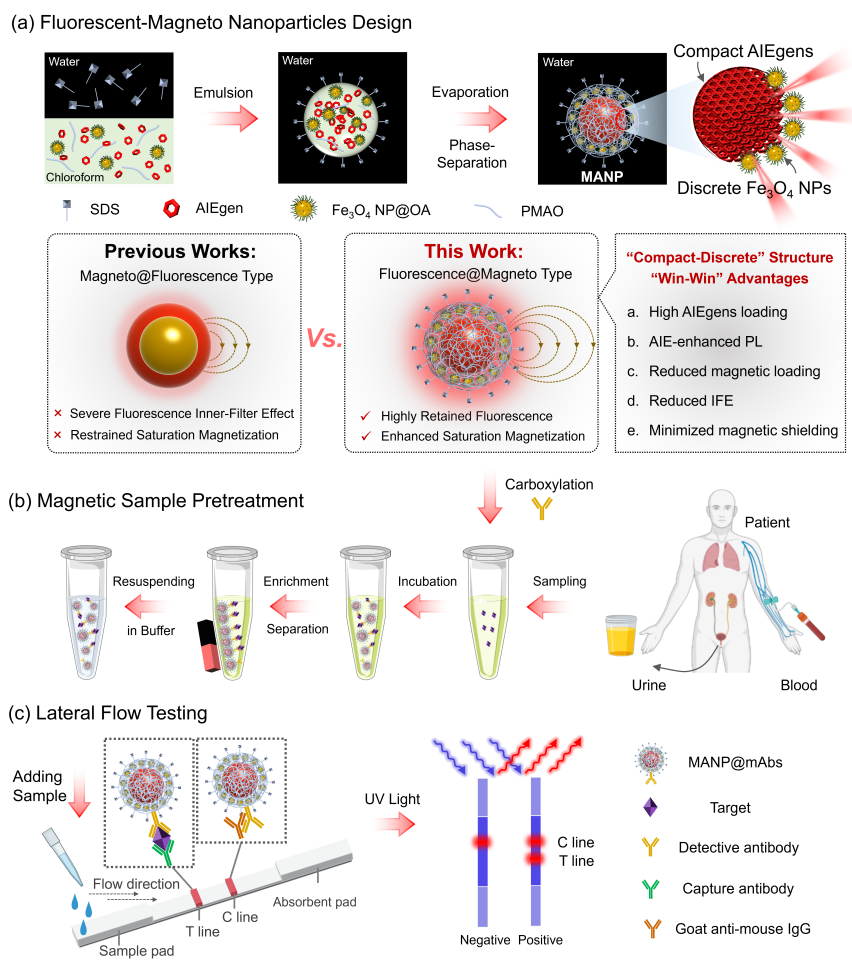
Scheme 1. Schematic of (a) the construction process of the MANP, (b) the magnetic pretreatment of blood and urine samples using the MANP nanoprobe, and (c) the mechanism of the MANP-based LFIA for ultrasensitive POCT detection.
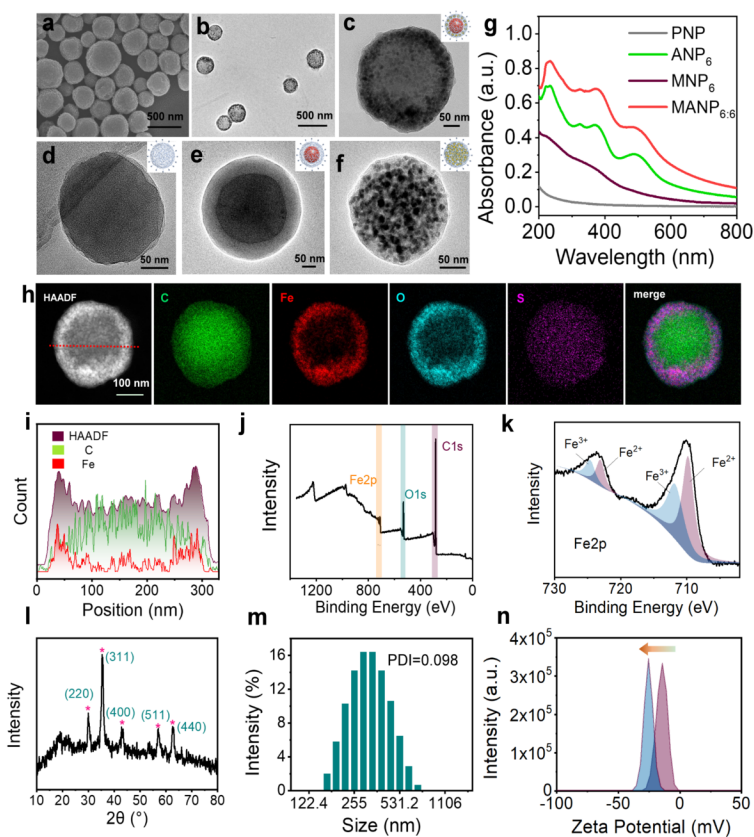
Figure 1. (a) SEM image, (b) TEM image, and (c) magnified TEM image of MANP$_{6:6}$. Magnified TEM images of (d) PNP, (e) ANP$_6$, and (f) MNP$_6$. The insets show structural illustrations of the nanoparticles. (g) UV–vis spectra of PNP, ANP$_6$, MNP$_6$, and MANP$_{6:6}$. (h) EDX elemental mapping images of C, Fe, O, and S on MANP$_{6:6}$, along with the merge image. (i) EDX line scan across the center of MANP$_{6:6}$, showing the atomic relative counts of C and Fe. (j) XPS spectrum of MANP$_{6:6}$ and (k) high-resolution XPS spectrum of Fe 2p. (l) XRD pattern of MANP$_{6:6}$. (m) Hydrodynamic size distribution of MANP$_{6:6}$. (n) Zeta potential evolution of MANP$_{6:6}$ before and after carboxylation.

14
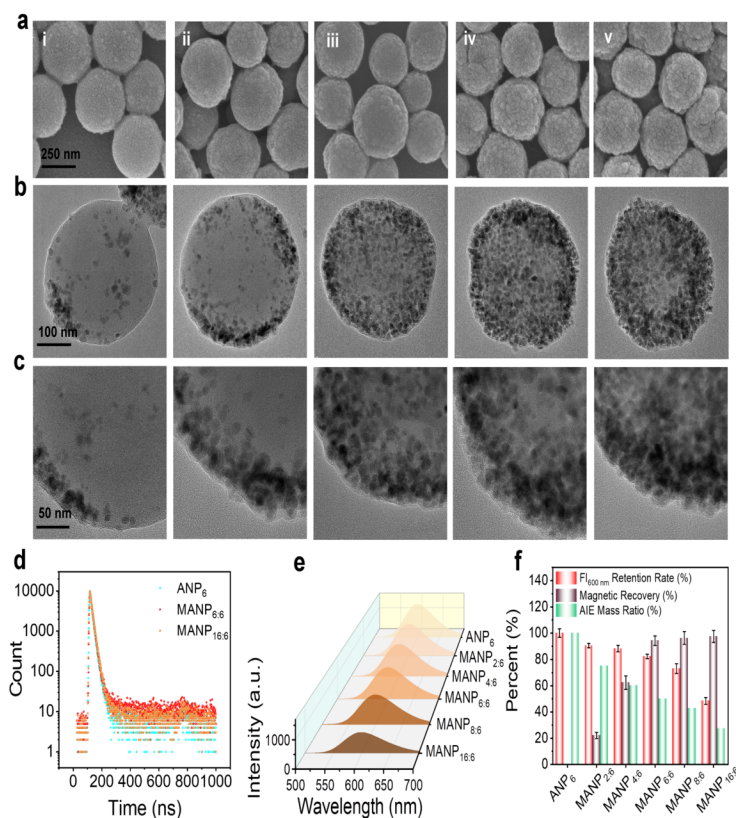
Figure 2. (a) SEM images, (b) TEM images, and (c) Magnified TEM images of (i) $MANP_{2:6}$, (ii) $MANP_{4:6}$, (iii) $MANP_{6:6}$, (iv) $MANP_{8:6}$, and (v) $MANP_{16:6}$. (d) Fluorescent lifetimes of ANP_6, $MANP_{6:6}$, and $MANP_{16:6}$. (e) Fluorescent spectra and (f) Fluorescence retention rate, magnetic recovery, and AIE mass ratio of MANP at different feeding amounts of $Fe_3O_4NPs@OA$.
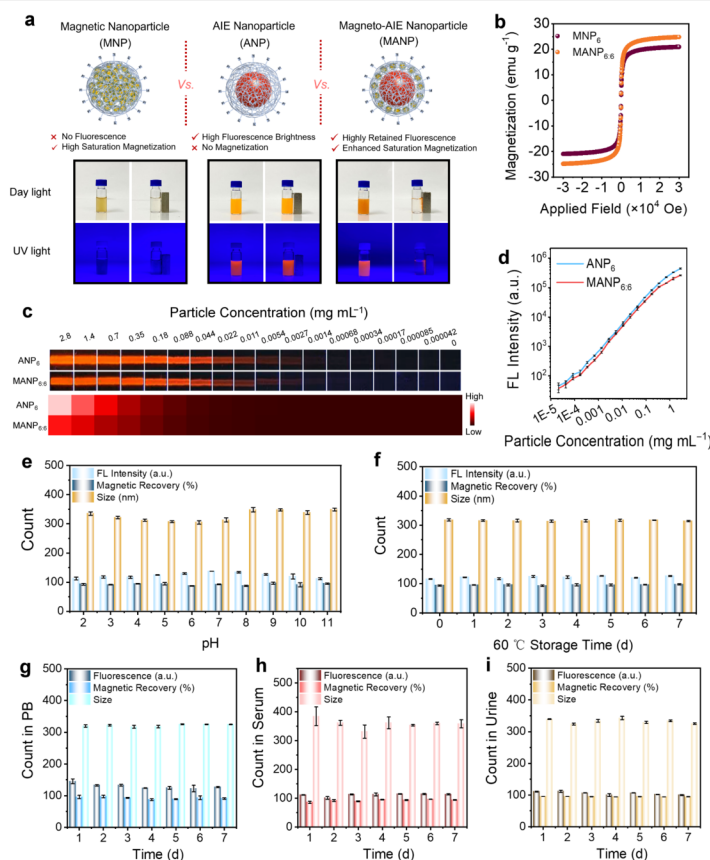
Figure 3. (a) Structural and performance illustration of MNP_6, ANP_6, $MANP_{6:6}$, and actual photographs of MNP_6, ANP_6, $MANP_{6:6}$ with/without applying an external magnetic field under day light and UV light. (b) Magnetic hysteresis loops of MNP_6 and $MANP_{6:6}$ obtained on a SQUID system at 300 K. (c) Fluorescence photos of ANP_6 and $MANP_{6:6}$ and the corresponding color maps in different particle concentrations. (d) Fluorescent intensities of different concentrations of ANP_6 and $MANP_{6:6}$ sprayed on paper strips. (e) Fluorescent intensity, magnetic recovery, and hydrodynamic size of $MANP_{6:6}$ dispersed in aqueous solutions with pH values ranging from 2 to 11. (f) Fluorescent intensity, magnetic recovery, and hydrodynamic size of $MANP_{6:6}$ stored in water at 60 °C for 7 days. Fluorescent intensity, magnetic recovery, and hydrodynamic size of $MANP_{6:6}$ incubated in (g) 10 mM PB (pH 7.4), (h) human serum, and (i) human urine for 7 days.
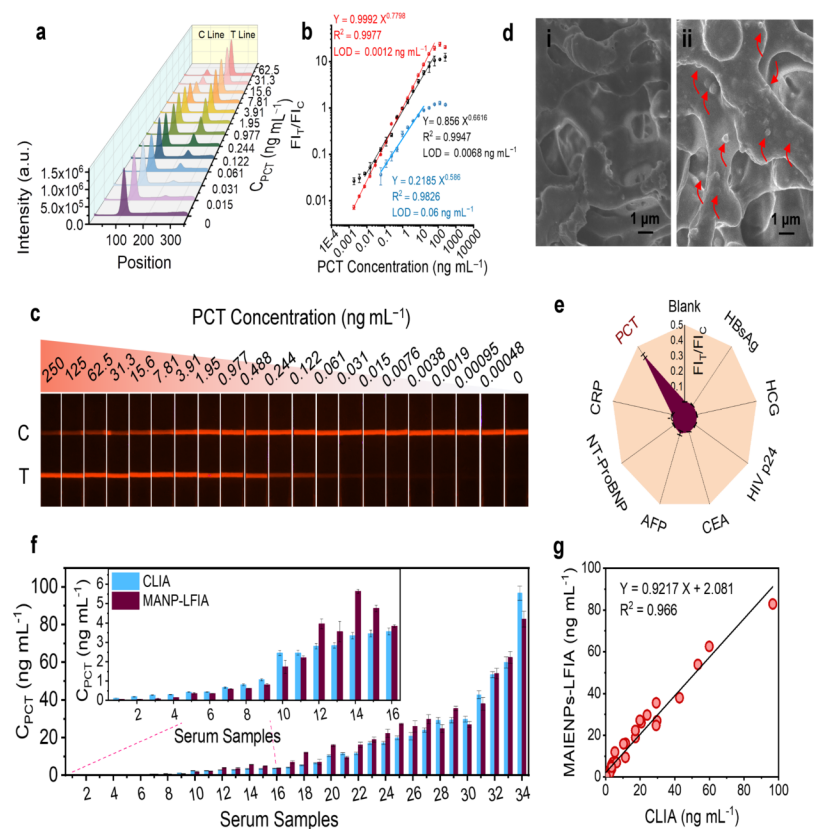
Figure 4. (a) Integrated scanning curves of MANP-FLIA with different PCT concentrations in serum. (b) Calibration curves of MANP-FLIA with magnetic operation (red), MANP-FLIA without magnetic operation (black), and AuNPs-LFIA (blue) with different PCT concentrations in serum. (c) Fluorescent photographs of MANP-FLIA test strips in response to different concentrations of PCT in serum after magnetic enrichment and separation (0–250 ng mL⁻¹). (d) SEM images of the T line region on the NC membrane after running with MANP$_{6:6}$@mAbs at PCT concentrations of (i) 0 ng mL⁻¹ and (ii) 100 ng mL⁻¹. (e) Specificity evaluation of the proposed MANP-FLIA platform toward various inspected species. The concentration of PCT is 1 ng mL⁻¹, and the concentration of all the other interfering species is 1000 ng mL⁻¹. (f) Comparison of the proposed MANP-FLIA method with the standard clinical CLIA method in actual serum samples. (g) Correlation analysis between the proposed method and the standard CLIA method.
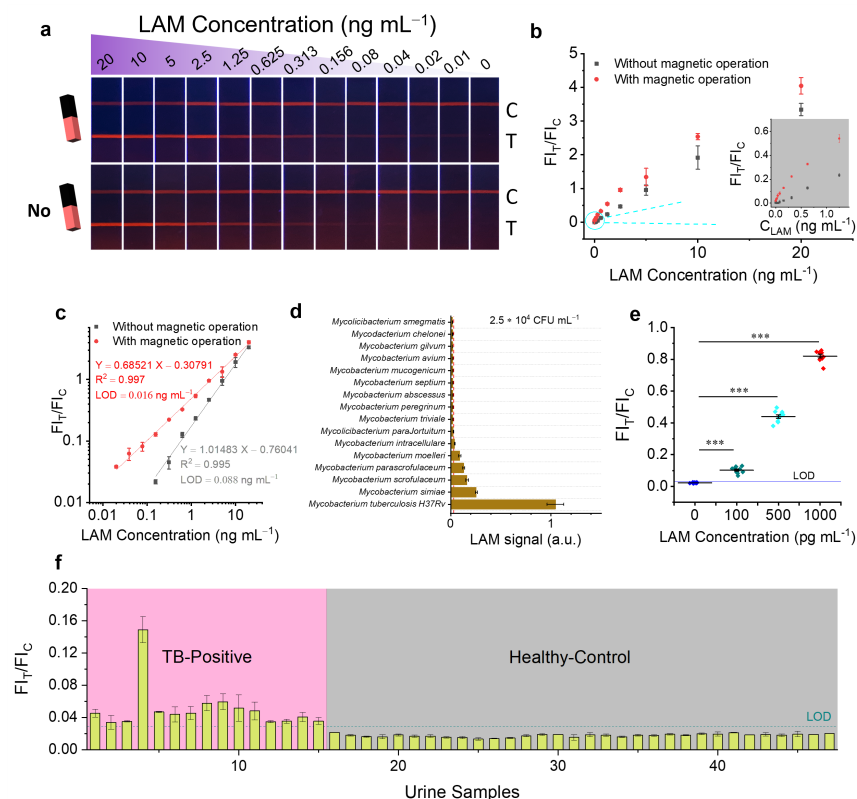
Figure 5. (a) Fluorescent photographs, (b) signal responses, and (c) calibration curves of MANP-FLIA test strips in response to different concentrations of LAM (0–20 ng mL^{-1}) in urine with/without magnetic enrichment and separation. (d) Specificity evaluation of the proposed MANP-FLIA platform toward various mycobacteria species with a bacterial concentration of 2.5×10^4 CFU mL^{-1}. (e) Fluorescent signal of MANP-FLIA when adding different concentration levels of LAM into urine samples provided by 10 individual healthy people. (f) Diagnosis result of clinical TB-positive patients and healthy individuals obtained using MANP-FLIA.

The table of contents entry:
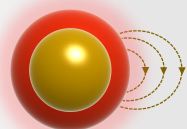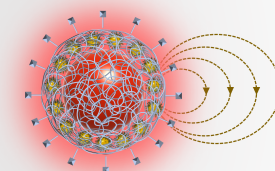
A new compact-discrete spatial arrangement is introduced on a "fluorescence@magneto" core-shell nanostructure with a close-packed AIEgen core and a meager magnetic shell. The rational design endows the magneto-AIE nanoparticle (MANP) with "win-win" performances: highly retained fluorescent intensity and remarkedly enhanced magnetic activity. The MANP demonstrates great potential in ultrasensitive point-of-care bacterial infection diagnosis on the immunochromatographic assay platform.

Keywords: fluorescent-magneto, aggregation-induced emission, self-assembly, point-of-care test, bacterial infection diagnosis

Authors: Yu Su[1, 2], Xirui Chen[1, 2], Huan Huang[4, 5], Yuhao Wu[1, 2], Xuanang Shen[1, 2], Xiangkai Lin[1, 2], Kun Sun[1, 2], Xiao-Yong Fan[4, *], Xiaolin Huang[1, 2, *] and Yonghua Xiong[1, 2, 3, *]

Title: Rearranging Fluorescence-Magneto Spatiality for "Win-Win" Dual Functions to Enhance Point-of-Care Diagnosis